

Bursting Oscillations during Metal Electrodeposition: Experiments and Model

Levent Organ, István Z. Kiss, and John L. Hudson*

Department of Chemical Engineering, 102 Engineers' Way, University of Virginia, Charlottesville, Virginia 22904-4741

Received: March 31, 2003; In Final Form: May 2, 2003

Experiments were carried out on bursting oscillations in an electrochemical system, the dissolution of iron in sulfuric acid. Bursting characteristics were investigated as functions of the parameters applied potential and external resistance. We develop a model that incorporates the effects of oxide and salt films. This model reproduces all the important features of the dynamics seen in experiments including both the slow active–passive oscillations and the faster oscillations on the mass-transfer-limited plateau as well as the bursting phenomena. During this bursting, two time scales are important: the slow variation of the salt-film thickness and the faster dynamics of a three-variable (potential drop and proton and iron(II) concentrations) subsystem.

1. Introduction

Bursting is a type of oscillatory behavior often observed in the electrical activity of biological membranes. The oscillations are characterized by a complex waveform in which a slow (often steady-state-like), “silent” dynamics is interrupted by fast, repetitive spiking (bursting).¹ A variety of waveforms have been observed in biological systems, for example, “parabolic” bursting of neuronal pacemakers,² “square wave” bursting of insulin secreting pancreatic β cells,^{3,4} or the “elliptic” bursting of rodent trigeminal interneurons.⁵ Some features of the bursting dynamics can be interpreted by dividing the variables into slow and fast depending on the time scales over which they vary.¹ A systematic characterization of bursting has been carried out on the basis of the bifurcation structure of the fast subsystem as a function of the (constant) slow variable.^{1,6} Several bursting waveforms, many not yet reported in experiments and realistic model equations, have been found.⁶

Although bursting was originally observed and studied in biological systems, it also occurs in a variety of physical⁷ and chemical systems. Mixed-mode oscillations have been observed in homogeneous chemical reactions, such as the BZ reaction;⁸ these can be considered to be a kind of bursting consisting of a mixture of small and large amplitude oscillations. Coupled reactors of chlorine dioxide–iodide oscillators show bursting waveforms reminiscent of a crab neuron.⁹ Chaotic bursting has been observed in a full-scale chlorination reactor;¹⁰ here the appearance of sustained oscillations can be used as an early warning sign of incipient reaction extinction, so that a detailed knowledge of reactor dynamics is of great importance. In electrochemical systems, bursting oscillations have been reported during H_2O_2 reduction on platinum,^{11,12} during iron dissolution in sulfuric acid with halogen additives,^{13–19} and with dichromate ions coupled with graphite or zinc electrodes.²⁰ A possible mechanism of bursting in electrochemical systems has been developed on the basis of a polarization scan with two negative slopes and a (hypothetical) slow variable.²¹ However, a detailed realistic model of bursting behavior in these electrochemical systems is not yet available.

In this paper experiments and modeling studies of bursting oscillations are carried out with electrodeposition of iron in

sulfuric acid solution. Iron electrodeposition has been long known to exhibit two regions of oscillations.²² Very fast, small amplitude, often chaotic oscillations occur on the mass-transfer-limited plateau of the polarization curve.^{23–28} At more anodic potentials, slow oscillatory cycles between the active and passive iron electrode occur.^{29–33} We study the effect of relatively large external resistance in series with the iron electrode on the dynamical behavior in the two regions. With appropriate resistance, the two regions overlap and bursting behavior arises. The dynamics are explored as a function of circuit potential and external resistance. The effects of electrolyte concentration and electrode size are also considered. We propose a simple model to simulate the rich dynamics of iron dissolution. Although many models have been developed to simulate the oscillatory dynamics,^{31,34–44} most treat the active–passive region, and thus they cannot be used to describe either the fast oscillations observed on the mass-transfer plateau or the bursting dynamics. We extend a model for active–passive oscillations⁴⁴ by adding the effect of a salt layer. This revised model yields both slow active–passive oscillations and fast oscillations on the mass-transfer-limited plateau. By treating the salt layer thickness as a (slow) variable, bursting oscillations develop. Numerical simulations of polarization scans with different resistors are presented and compared to the experiments. The characteristics of the bursting oscillations are further explored by treating the slow variable, the salt-film thickness, as a controlled parameter.

2. Experimental Procedure

Experiments were carried out in a three-compartment cell, which contained 550 mL of H_2SO_4 solution. Iron wires of 0.5 and 2.0 mm diameter (99.995% purity, metals basis, Alfa Aesar) were used. Each straight wire was first coated with epoxy and then embedded in an epoxy cylinder. The electrodes were polished in such a way that only the cross section of the wire was exposed to the solution. All potentials reported in this study are with respect to a $\text{Hg}/\text{Hg}_2\text{SO}_4$ reference electrode with a saturated K_2SO_4 salt bridge solution (Radiometer Analytical). The counter electrode was a platinum clad niobium expanded-mesh of 20 cm^2 surface area. The solutions were prepared from certified ACS plus grade H_2SO_4 (Fisher Scientific) and deionized H_2O .

* Corresponding author. E-mail: hudson@virginia.edu.

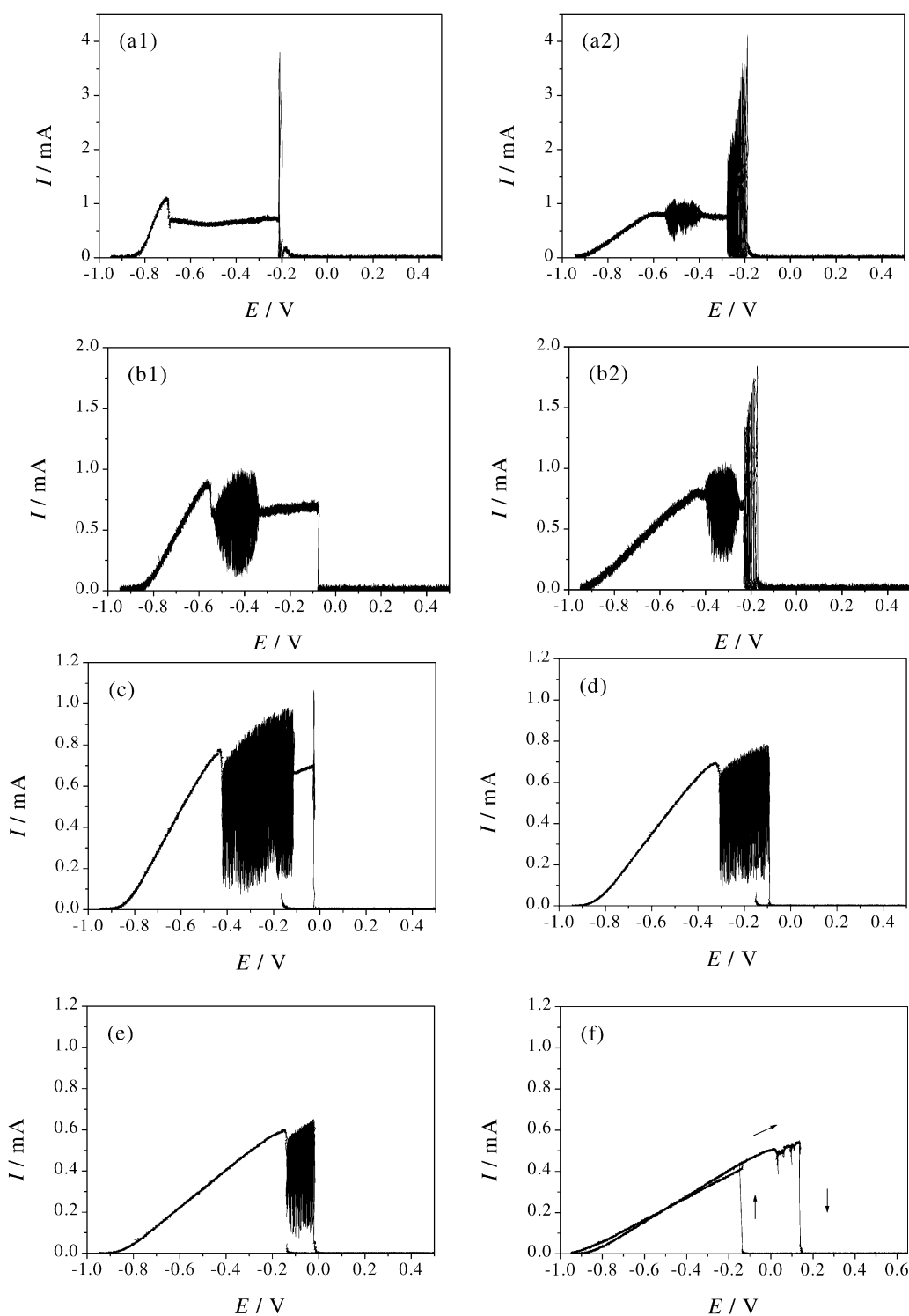


Figure 1. Experimental potential sweeps. 0.5 mm diameter Fe disk in 0.5 M H_2SO_4 . Sweep rate = 1 mV s^{-1} . (a1) positive sweep, $R_{\text{ext}} = 0 \Omega$; (a2) negative sweep, $R_{\text{ext}} = 0 \Omega$; (b1) positive sweep, $R_{\text{ext}} = 200 \Omega$; (b2) negative sweep, $R_{\text{ext}} = 200 \Omega$; (c) positive sweep followed by negative sweep until activation of the electrode, $R_{\text{ext}} = 400 \Omega$; (d) positive sweep followed by negative sweep until activation of the electrode, $R_{\text{ext}} = 600 \Omega$; (e) positive sweep followed by negative sweep until activation of the electrode, $R_{\text{ext}} = 1 \text{ k}\Omega$; (f) CV, $R_{\text{ext}} = 1.5 \text{ k}\Omega$; potentials in all figures are with respect to a $\text{Hg}/\text{Hg}_2\text{SO}_4$ reference electrode.

The solution was bubbled with nitrogen for 20 min before each experiment. The working electrode was wet polished by 240, 320, 400, 600, 800, and 1200 grit polishing papers. After the polishing, it was washed with deionized H_2O and placed into the solution in a downward facing position. The solution was stirred with a magnetic stirrer for 10 min to bring about temperature equilibrium at $293 \pm 0.5 \text{ K}$. The stirrer was turned off, and experiments were carried out under stagnant conditions.

A potentiostat (EG&G, Model 273) was used to control the potential (E) of the working electrode. Data were stored in a PC by means of a 32 Channel A/D board (Keithley DAS-1802HC) and data acquisition software (Snap Master, version 3.2). Cyclic voltammograms (CVs) were carried out to locate potential windows of current oscillations. In a CV the potential was scanned at 1 mV s^{-1} from -0.95 V to a more positive potential, followed by a reverse scan back to -0.95 V . Data

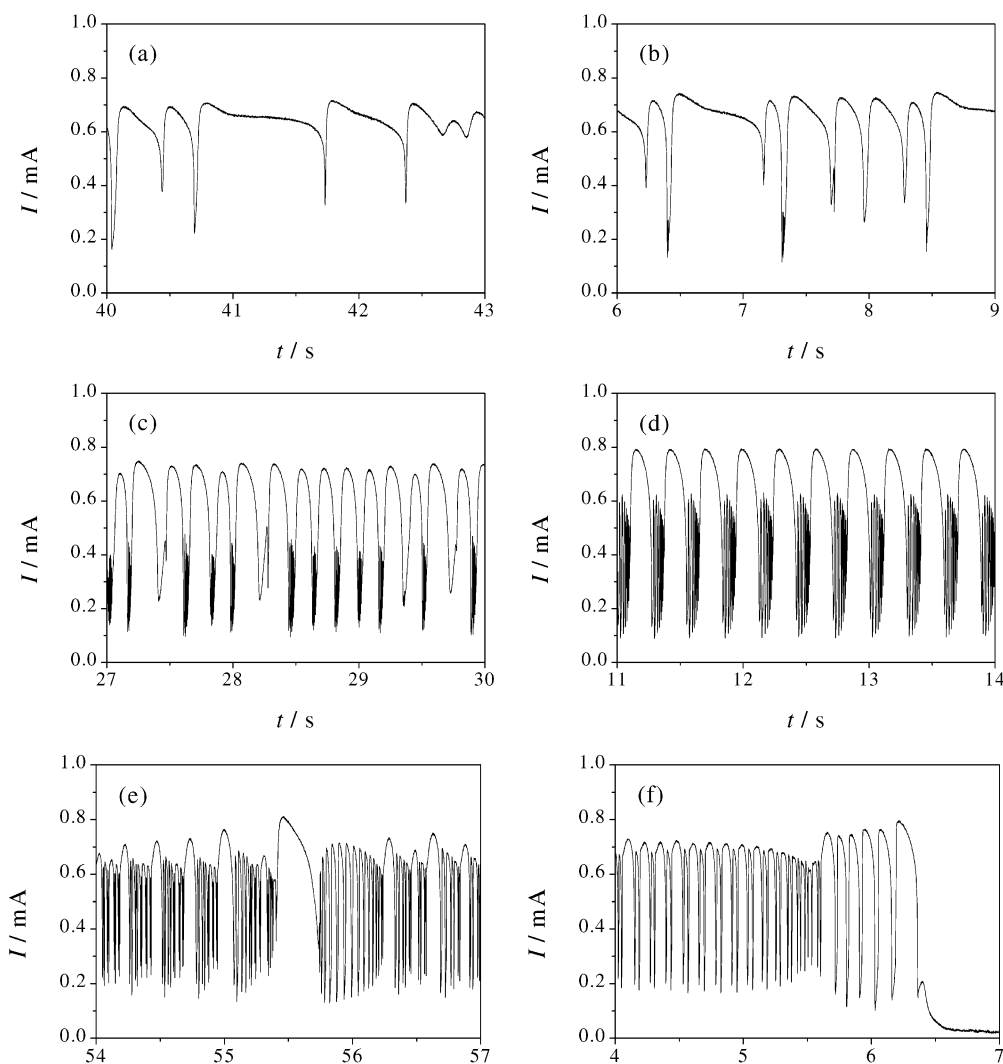


Figure 2. Experimental current time series segments during a slow positive sweep. 0.5 mm diameter Fe disk in 0.5 M H_2SO_4 . Sweep rate = 1 mV s^{-1} . $R_{\text{ext}} = 600 \Omega$. Corresponding average potentials: (a) -0.240 V ; (b) -0.214 V ; (c) -0.193 V ; (d) -0.148 V ; (e) -0.105 V ; (f) -0.095 V . These are the average potentials over the time interval of each figure.

were collected at a rate of 10 Hz. Once the ranges of oscillations are determined, further sweeps were carried out with faster data sampling rates (1000 Hz) in order to determine the type and the evolution of current oscillations in regions of interest. Current time series (also sampled at 1000 Hz) under potentiostatic conditions were recorded after scanning the potential from -0.95 V to the potential of interest at 1 mV s^{-1} . In most experiments, an external resistor was connected in series with the working electrode to induce current oscillations.

3. Experimental Results

Oscillations on the Mass-Transfer Plateau and in the Active–Passive Region. Figure 1 shows potential sweeps of a 0.5 mm diameter Fe disk in 0.5 M H_2SO_4 with different external resistors R_{ext} . Positive and negative sweeps at $R_{\text{ext}} = 0$ are given in Figure 1a1 and 1a2, respectively. In Figure 1a1 a maximum at -0.705 V is observed; the decrease of current above -0.705 V is typical of Fe electrodisolution in sulfuric acid and is attributed to the formation of a salt layer on the surface of the electrode.^{23,45} The region of almost constant current between -0.69 and -0.215 V is called the mass-transfer-limited plateau or the limiting-current plateau. At the end of the plateau, active–passive oscillations with high amplitude are observed over a narrow potential window (15 mV) before the passivation of the

electrode at -0.2 V . In the reverse sweep (Figure 1a2), the active–passive oscillations are observed over a wider potential range (85 mV) before the establishment of a limiting current. In Figure 1a2 a region of current oscillations of smaller amplitude in the mass-transfer-limited plateau between -0.395 and -0.54 V is also seen. Parts b1 and b2 of Figure 1 show positive and negative sweeps obtained with $R_{\text{ext}} = 200 \Omega$. In the positive sweep in Figure 1b1, oscillations appear between -0.52 and -0.34 V while the active–passive oscillations at the end of the mass-transfer-limited plateau disappear. It is also seen that the electrode passivates at a more positive potential (-0.075 V) compared to the case of Figure 1a1. From a comparison of the positive and negative sweeps, it is seen that a region of bistability forms between -0.23 and -0.075 V . This bistable region forms due to different magnitudes of IR potential drop in the positive and negative sweeps.^{46,47}

With a further increase of the external resistance to 400Ω (Figure 1c), both the oscillatory region on the plateau and the passivation potential shift in the positive direction because of the additional IR drop induced by the larger external resistor. The oscillation amplitude becomes larger with increase of potential; after the oscillatory region, the current continues to rise until passivation of the electrode at -0.025 V . Parts d and e of Figure 1 were obtained with $R_{\text{ext}} = 600 \Omega$ and $1 \text{ k}\Omega$,

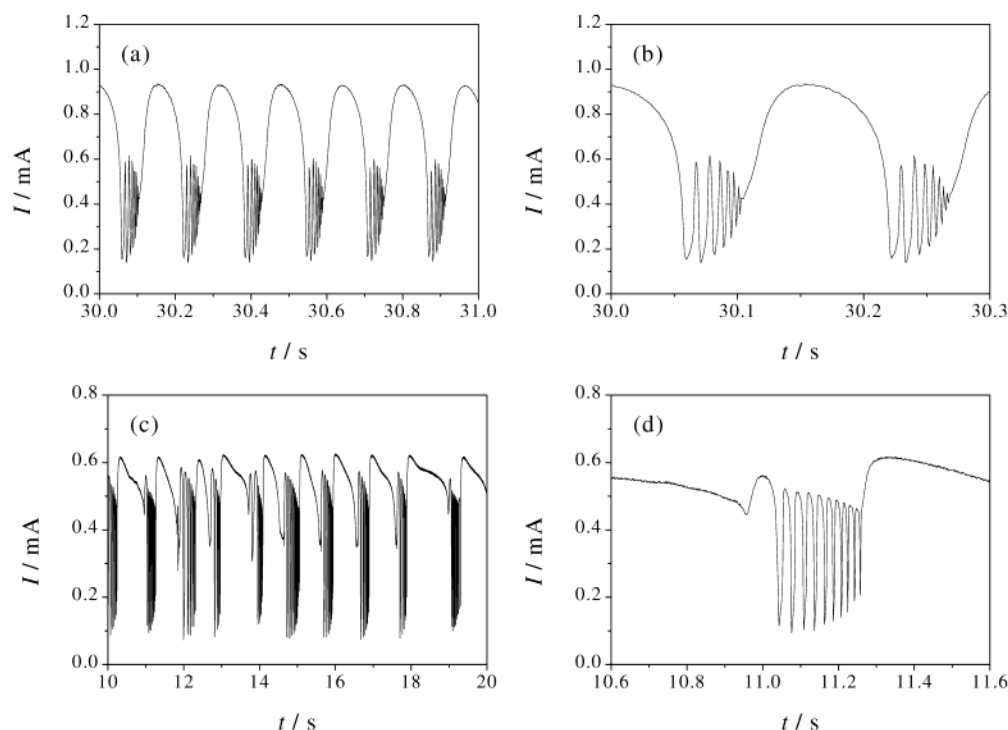


Figure 3. Experimental current time series. 0.5 mm diameter Fe disk in 0.5 M H_2SO_4 . (a) periodic bursting, $R_{\text{ext}} = 400 \, \Omega$, $E = -0.2$ V; (b) zoom on bursts seen in part a; (c) chaotic bursting, $R_{\text{ext}} = 1 \, \text{k}\Omega$, $E = -0.050$ V; (d) zoom on a burst seen in part c.

respectively. These two CVs differ from those with smaller resistors in that the mass-transfer-limited plateau oscillations cease with the passivation of the electrode. It is also seen that with $1 \, \text{k}\Omega$ (Figure 1e) the oscillations begin at a higher potential (-0.135 V) and the oscillatory range is narrower. The oscillatory region disappears in the positive sweep with $R_{\text{ext}} = 1.5 \, \text{k}\Omega$ (Figure 1f).

Bursting Dynamics. Figure 2 shows waveforms of the current oscillations during a very slow ($1 \, \text{mV s}^{-1}$) positive sweep with a $600 \, \Omega$ resistor. (Over the interval of each time series the potential changed only a few millivolts.) The experimental parameters are the same as those of Figure 1d. The oscillations at the beginning of the oscillatory region seen in Figure 1d are chaotic. An example is given in Figure 2a, which shows the oscillation waveform at around -0.240 V. As the potential becomes more positive, small bursts at the oscillation minima appear (Figure 2b). These bursts become more frequent and higher in amplitude later in the sweep, resulting in irregular bursting oscillations, a typical example of which is shown in Figure 2c. At more positive potentials, there is a narrow potential range where bursting oscillations are periodic at around -0.148 V (Figure 2d). After this region of regular bursting, the waveform becomes irregular again and oscillations with longer bursts are seen (Figure 2e). Figure 2f shows the time series just before passivation.

The development of bursting oscillations was also observed at somewhat lower (e.g., $R_{\text{ext}} = 400 \, \Omega$) and higher (e.g., $R_{\text{ext}} = 1000 \, \Omega$) resistances. At $R_{\text{ext}} = 400 \, \Omega$, periodic bursting oscillations occurred in a wider potential region; a potentiostatic current–time series is shown in Figure 3a and b. With $R_{\text{ext}} = 1000 \, \Omega$ bursts formed as soon the current started to oscillate, and only irregular bursting oscillations were observed. An example is presented in Figure 3c; a zoom of a burst is shown in Figure 3d.

Higher H_2SO_4 Concentration. Figure 4a shows a positive sweep at a higher H_2SO_4 concentration and $R_{\text{ext}} = 1.2 \, \text{k}\Omega$. Small bursts form at the oscillation minima soon after the start of

oscillations. The bursting is at first irregular and then more regular at more positive potentials. As opposed to the experiments with 0.5 M H_2SO_4 , regular bursting is not limited to a narrow potential range but it prevails until the passivation of the electrode. The period of the regular bursting oscillations becomes longer as the potential is increased. This period lengthening is illustrated by two potentiostatic current–time series taken inside the oscillatory range of Figure 4a. Parts b and c of Figure 4 show the time series at -0.049 and -0.008 V, respectively. The oscillations in Figure 4c have a longer period compared to that for those of Figure 4b.

Results of experiments with $R_{\text{ext}} = 1 \, \text{k}\Omega$ are presented in Figure 5. The two results shown in Figure 5a and b were obtained at the same conditions; the variation in the behavior is likely caused by heterogeneities of the electrode surface and/or variations of the properties of the salt film caused by small differences in conditions. In some experiments, the electrode passivated at 0 V (Figure 5a), while, in others, passivation took place at considerably higher potentials (Figure 5b). When the surface passivated at 0 V as in Figure 5a, chaotic oscillations without bursts, irregular bursting oscillations, and regular bursting oscillations were seen successively as the potential was scanned in the positive direction. These results are similar to those obtained with higher resistance. During the sweep shown in Figure 5b, the electrode passivated at about 0.2 V; passivation takes place from a nearly steady state rather than from an oscillatory state as in Figure 5a. Moreover, the system exhibits oscillations with relatively small amplitude between -0.02 and 0.2 V in Figure 5b. In Figure 5c and d, expanded segments of these small amplitude oscillations are shown. In Figure 5c, oscillations such as typically seen on the mass-transfer plateau alternate with very small amplitude, high frequency oscillations. At higher potentials, high frequency, small amplitude oscillations alternate with nonoscillatory behavior, as shown in Figure 5d. At potentials higher than about 0.05 V, the current undergoes very slow fluctuations around the limiting value; further increase in potential leads to passivation.

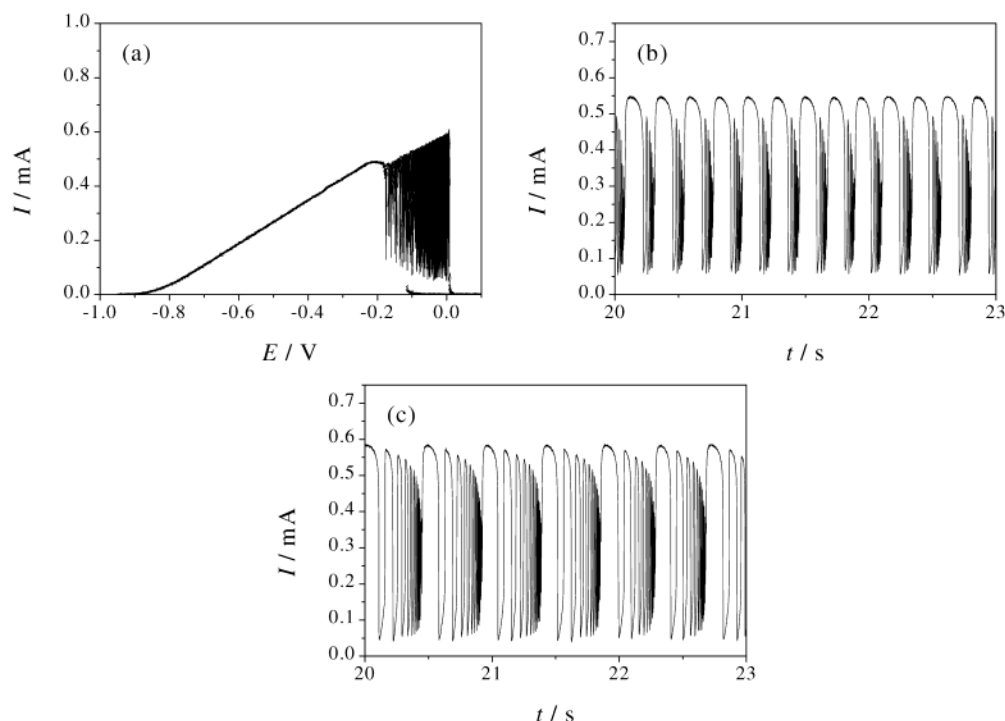


Figure 4. Experimental current time series. 0.5 mm diameter Fe disk in 1 M H_2SO_4 . $R_{\text{ext}} = 1.2 \text{ k}\Omega$. (a) positive sweep followed by negative sweep until activation of the electrode, sweep rate = 1 mV s^{-1} ; (b) current time series at -0.049 V ; (c) current time series at -0.008 V .

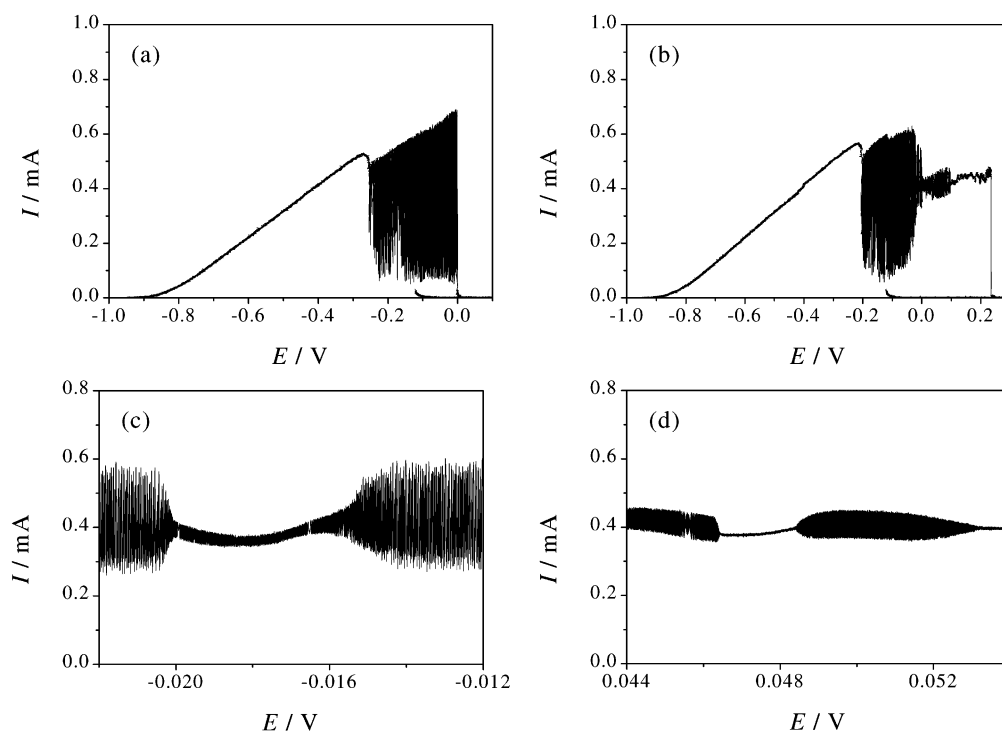


Figure 5. Experiments with a 0.5 mm diameter Fe disk in 1 M H_2SO_4 . $R_{\text{ext}} = 1 \text{ k}\Omega$. Sweep rate = 1 mV s^{-1} . (a and b) positive sweeps followed by negative sweep until activation of the electrode; (c and d) segments of a positive sweep.

Larger Surface Area. Bursting behavior was also found with a larger Fe disk electrode ($d = 2.0 \text{ mm}$). In general, the behavior is more complicated with this larger electrode. Since the current is about 16 times larger than that with a 0.5 mm diameter electrode, about 16 times smaller resistors were used. A CV in 1 M H_2SO_4 is shown in Figure 6a with $R_{\text{ext}} = 50 \Omega$. Although both irregular and regular bursting oscillations were seen with 50Ω , the regular bursting has a more complicated waveform, as shown in Figure 6b; every second group of bursts is the same.

The first burst has alternately a relatively large amplitude. When the external resistance is increased to 60Ω , only irregular bursting is seen in the positive sweep (Figure 6c and d). Although the bursting oscillations are irregular, the time series may contain short segments with periodic-like oscillations, as exemplified in Figure 6d.

The iron system also exhibits excitability, as shown in Figure 7. At a fixed potential of 0.051 V (about 25 mV above the passivation potential), with other conditions the same as those

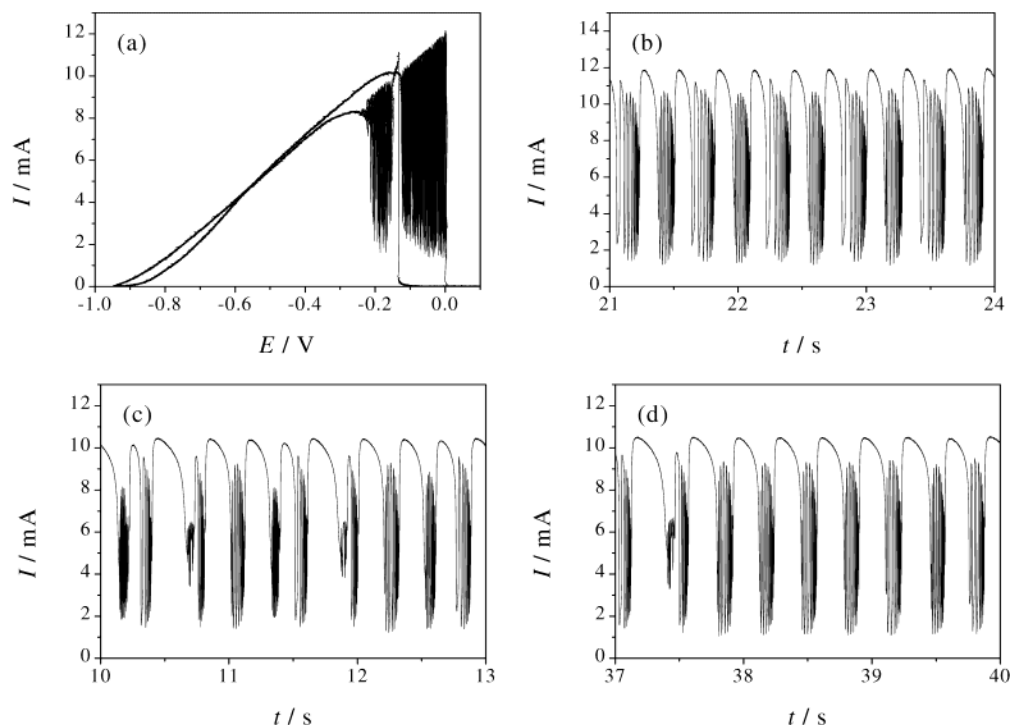


Figure 6. Experiments with a 2.0 mm diameter Fe electrode in 1 M H_2SO_4 . (a) CV at 1 mV s^{-1} , $R_{\text{ext}} = 50 \Omega$; (b) time series segment during a slow positive sweep at 1 mV s^{-1} , $R_{\text{ext}} = 50 \Omega$ (average potential over the time interval shown is -0.014 V); (c) time series, $R_{\text{ext}} = 60 \Omega$, $E = -0.010 \text{ V}$; (d) short regular bursting oscillation within the irregular bursting time series illustrated in part c.

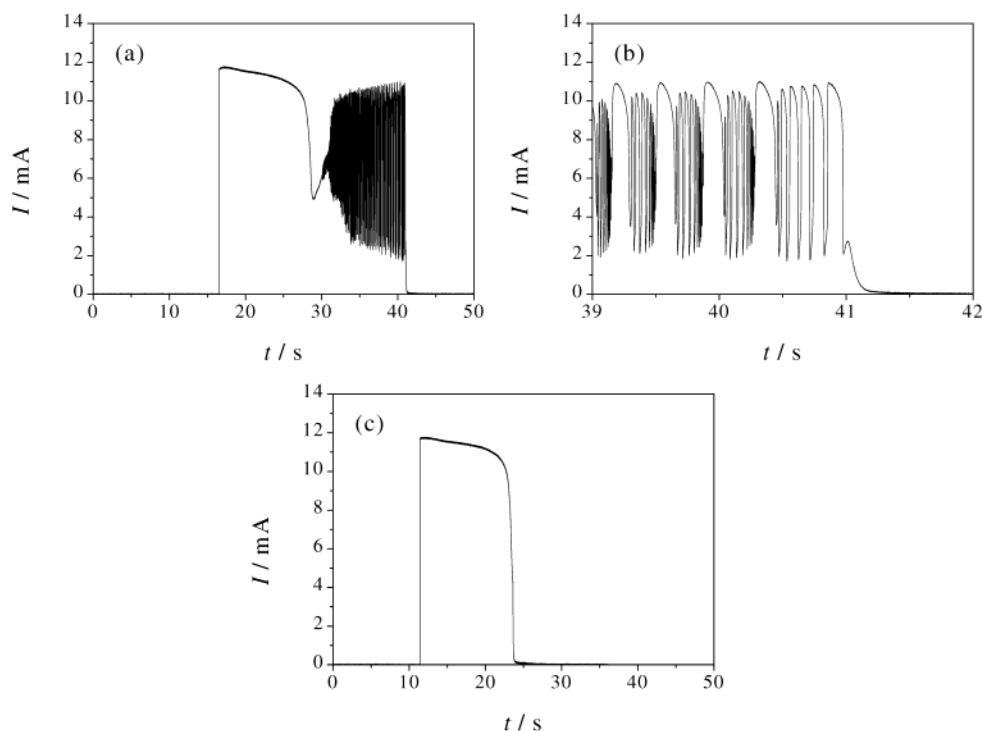


Figure 7. Experiment on excitability. 2.0 mm diameter Fe electrode. 1 M H_2SO_4 . $R_{\text{ext}} = 60 \Omega$. A pulse was imposed on the passive state at 0.051 V by changing the potential to open circuit conditions from $t = 13.2 \text{ s}$ to $t = 16.5 \text{ s}$. (a) current time series; (b) zoom on the end of the oscillatory time series in part a showing the bursting oscillation and the repassivation of the electrode; (c) current time series for a subsequent similar perturbation.

in Figure 6c, a single (passive) stable steady-state exists. A small perturbation in potential results in a small increase in current followed by a simple, fast transient return to the stable steady state. A larger perturbation, here applied via a short change in the potential to open circuit conditions, yields a long transient. The current response is shown in Figure 7a. Immediately after the perturbation, a large current peak and subsequent transient oscillations were observed. These are mainly bursting oscilla-

tions; Figure 7b illustrates the oscillation just before the repassivation of the electrode. A subsequent perturbation applied after repassivation produces a large excursion without oscillations, as seen in Figure 7c.

4. Simulations

Model. Iron dissolution is a classic example of an oscillatory electrochemical system. Franck and FitzHugh proposed a simple

two-variable model that qualitatively describes the active-passive oscillatory cycles.³¹ Two important factors are the migration current of H^+ ions and the Flade potential that depends on the H^+ concentration. The importance of ohmic drop was later recognized and incorporated in the models.^{21,34,39,48,49} A two-variable model has been recently used⁴⁴ to interpret spatiotemporal patterns in the active-passive dissolution region:

$$C_d \frac{d\phi}{dt} = \frac{E - \phi}{R_s} - j_F(\phi, h) \quad (1a)$$

$$\frac{dh}{dt} = \frac{2D_h}{\delta^2}(h_0 - h) - \frac{2}{\delta}\mu_h h \frac{E - \phi}{R_s} \quad (1b)$$

$$j_F = \frac{A}{1 + \exp(\alpha(\phi - E_{\text{Flade}}(h)))} \quad (1c)$$

where ϕ is the potential drop over the double layer, h is the hydrogen ion concentration on the electrode surface, C_d is the double layer capacitance per surface area, E is the circuit potential, R_s is the series resistance of the cell, j_F is the Faradaic current density, δ is the thickness of the Nernstian diffusion layer, D_h is the diffusion coefficient of protons, h_0 is the bulk H^+ concentration, and μ_h is a migration coefficient of protons. The current density is obtained from $(E - \phi)/R_s$. Equation 1a is the charge balance; eq 1b is the mass balance for H^+ considering only diffusion and migration. The Faradaic current (eq 1c) is a smoothed Heaviside function of ϕ : at large potentials the current sharply decreases due to oxide film formation. h changes the inflexion point of the smoothed Heaviside curve, simulating the H^+ concentration dependent Flade potential (E_{Flade}).

We incorporate the effects of the salt film into the model of eq 1 in order to reproduce the oscillations on the mass-transfer-limited plateau as well as the bursting oscillations. (Newman et al.^{36,38} and Koper³⁹ have previously considered the effect of a salt film on the active-passive transition.) The Faradaic current (the last term of eq 1a) is made dependent on the coverage of both the oxide and salt films. We assume that the oxide layer coverage, Θ_{ox} , is a smoothed Heaviside function:

$$\Theta_{\text{ox}} = \begin{cases} 0 & \text{if } \phi \leq E_{\text{Flade}} \\ 1 - \exp(-50(\phi - E_{\text{Flade}})^2) & \text{otherwise} \end{cases} \quad (2)$$

Above the (hydrogen ion concentration h dependent) Flade potential⁵⁰

$$E_{\text{Flade}} = F1 + F2 \log(h) \quad (3)$$

the oxide layer forms. An expression similar to that used for the oxide layer is assumed for the salt-film layer coverage θ_{salt} :

$$\theta_{\text{salt}} = \begin{cases} 0 & \text{if } \phi \leq E_{\text{salt}} \\ (1 - \theta_{\text{ox}})(1 - \exp(-50(\phi - E_{\text{salt}})^2)) & \text{otherwise} \end{cases} \quad (4)$$

where E_{salt} is the potential at which salt-film formation starts. The salt film grows only on the surface not covered by oxide ($1 - \theta_{\text{ox}}$); thus, the breakdown of the salt film and the buildup of the oxide layer are parallel processes. The Faradaic current density is obtained from the dissolution of the free metal surface ($1 - \theta_{\text{ox}} - \theta_{\text{salt}}$) and current through the porous salt film:

$$j_F(e, h, c, \theta_{\text{salt}}, \theta_{\text{ox}}) = (1 - \theta_{\text{salt}} - \theta_{\text{ox}})k_1 \exp(b(\phi - E_0)) + k_2 \epsilon \theta_{\text{salt}} \quad (5)$$

where E_0 is the standard potential and k_1 , k_2 , and b are kinetic parameters. The porosity of the salt film, ϵ , is a function of the surface concentration of iron(II), c :

$$\epsilon = \begin{cases} 0.999 & \text{if } c \leq c_{\text{sat}} \\ 0.9 \exp(-0.5(c - c_{\text{sat}})^2) + 0.099 & \text{otherwise} \end{cases} \quad (6)$$

where c_{sat} is the saturation concentration of the salt film.³⁸ The concentration dependent porosity is an important characteristic of the salt film and, as we shall see below, leads to the fast oscillations on the mass-transfer-limited plateau.

The model of metal dissolution is described by the following variables: potential drop through the double layer (ϕ), surface iron(II) concentration (c), surface hydrogen ion concentration (h), and salt layer thickness (l). The following set of four ordinary differential equations is used:

$$C_d \frac{d\phi}{dt} = \frac{E - \phi}{R_{\text{eff}}(l)} - j_F(\phi, h, c, \theta_{\text{salt}}, \theta_{\text{ox}}) \quad (7a)$$

$$\frac{dh}{dt} = \frac{2D_h}{\delta^2}(h_0 - h) - \frac{2}{\delta}\mu_h h \frac{E - \phi}{R_{\text{eff}}(l)} \quad (7b)$$

$$\frac{dc}{dt} = \frac{2j_F(\phi, h, c, \theta_{\text{salt}}, \theta_{\text{ox}})}{\delta q_F} - \frac{2D_c}{\delta^2}c - \frac{2}{\delta}\mu_c c \frac{E - \phi}{R_{\text{eff}}(l)} \quad (7c)$$

$$(1 - \epsilon) \frac{dl}{dt} = k_{\theta} \theta_{\text{salt}} - k_l l \quad (7d)$$

Equation 7a is the charge balance. $R_{\text{eff}}(l)$ is the series resistance of the cell. The series resistance consists of two parts: the sum of electrolyte and external resistances (R_0) and the resistance of the salt layer:

$$R_{\text{eff}}(l) = R_0 + R_{\text{salt}} l \quad (8)$$

where R_{salt} is the resistivity of the porous salt film. The current density is $[E - \phi]/R_{\text{eff}}(l)$. Equations 7b and 7c are material balances for surface hydrogen ion and iron(II) ion. Both balances neglect transport effects such as convection near the stagnant electrode. The proton material balance (eq 7b) incorporates diffusion and migration but neglects the chemical terms due to oxide formation and hydrolysis of the salt film. The three terms on the right-hand side of eq 7c are a source term proportional to the Faradaic current (proportionality factor q_F), diffusion, and migration, respectively. Equation 7d describes the simplified kinetics of porous salt-film formation including first-order formation and dissolution.

Equations 7a–d were solved using the Gear method.⁵¹ The following physical and chemical constants were used: $C_d = 100 \mu\text{F cm}^{-2}$, $\delta = 0.01 \text{ cm}$, $D_h = 5 \times 10^{-5} \text{ cm}^2 \text{ s}^{-1}$, $D_c = 2.5 \times 10^{-5} \text{ cm}^2 \text{ s}^{-1}$, $\mu_h = 0.5 \text{ A}^{-1} \text{ s}^{-1} \text{ cm}^3$, $\mu_c = 0.025 \text{ A}^{-1} \text{ s}^{-1} \text{ cm}^3$, $q_F = 4 \text{ A s mol}^{-1} \text{ dm}^3 \text{ cm}^{-3}$, $b = 5$, $k_1 = 0.06 \text{ A cm}^{-2}$, $E_0 = -1 \text{ V}$, $k_2 = 0.1 \text{ A cm}^{-2}$, $F1 = -0.54 \text{ V}$, $F2 = 0.15 \text{ V}$, $E_{\text{salt}} = -0.99 \text{ V}$, $c_{\text{sat}} = 3 \text{ mol dm}^{-3}$, $R_{\text{salt}} = 150 \Omega \text{ cm}$, $k_{\theta} = 10^{-4} \text{ cm s}^{-1}$, $k_l = 0.01 \text{ s}^{-1}$, and $h_0 = 1 \text{ mol dm}^{-3}$. We note that the values of these parameters were determined to obtain a polarization curve at low resistance similar to that seen in the experiments; the model is meant to be a qualitative representation of the dynamics although many of the parameters do have realistic magnitudes. The salt layer thickness (l) serves as the slow variable in this system: k_{θ} and k_l are small numbers, reflecting the slow change of salt-film thickness during the dissolution process. The main purpose of modeling is to show

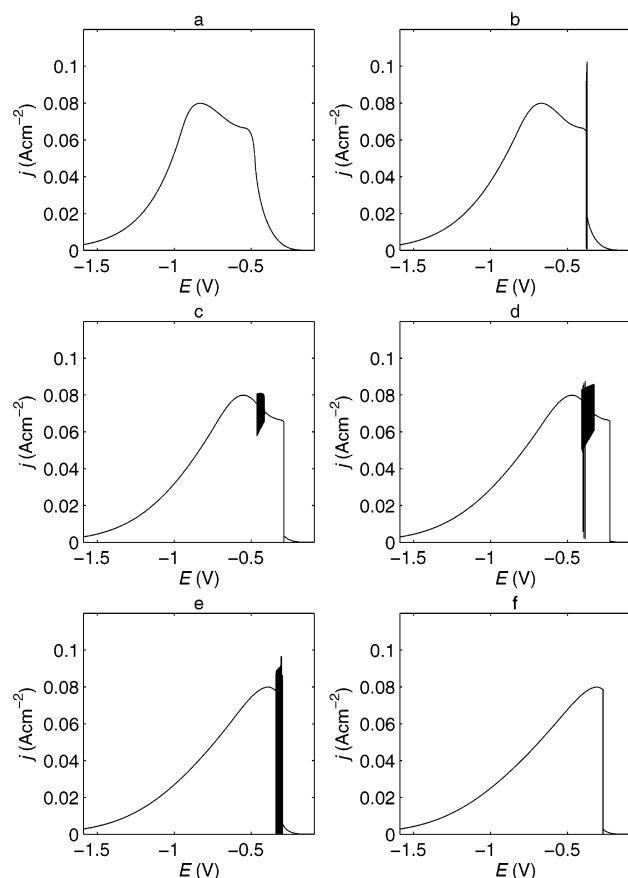


Figure 8. Simulated forward polarization scans at 0.25 mV s^{-1} with different series resistance: (a) $R_0 = 0.5 \Omega \text{ cm}^2$; (b) $R_0 = 2.5 \Omega \text{ cm}^2$; (c) $R_0 = 4 \Omega \text{ cm}^2$; (d) $R_0 = 5 \Omega \text{ cm}^2$; (e) $R_0 = 6 \Omega \text{ cm}^2$; (f) $R_0 = 7 \Omega \text{ cm}^2$.

the effect of the slow variable, l , on the dynamical behavior. In the simulations below, we investigate the behavior as a function of circuit potential (E) for different values of series resistance, R_0 , with all other parameters being held constant.

Polarization Scans. Polarization scans obtained at various series resistances R_0 are shown in Figure 8. At very low resistances (Figure 8a, $R_0 = 0.5 \Omega \text{ cm}^2$) the current density increases exponentially with circuit potential until about $E = -0.9 \text{ V}$. Above it, salt-film formation sets in, and due to the decreasing porosity of the film, the current decreases slightly. At about $E = -0.5 \text{ V}$ the electrode passivates and the current drops to low values. Oscillations are not observed. With increasing resistance (Figure 8b, $R_0 = 2.5 \Omega \text{ cm}^2$), however, large amplitude oscillations between the active and passive states develop. The active–passive oscillatory region disappears above $R_0 = 3 \Omega \text{ cm}^2$. At $R_0 = 4 \Omega \text{ cm}^2$ (Figure 8c), a new oscillatory region occurs in the mass-transfer-limited region; these oscillations have small amplitudes and do not involve passivation of the electrode. At larger resistance ($4 \Omega \text{ cm}^2 \leq R_0 \leq 6.5 \Omega \text{ cm}^2$; Figure 8d and e), the oscillations in the mass-transfer-limited region are a mixture of small amplitude and large amplitude oscillations. With even larger resistance ($R_0 \geq 7 \Omega \text{ cm}^2$; Figure 8f), no oscillations are observed; the electrode passivates before any mass-transfer or active–passive oscillations can develop. The model reproduces the effect of resistance on the shape of the polarization curve and the nature and location of the oscillations seen in the experiments, as shown in Figure 1.

Thus, we see a variety of types of dynamical behavior as a function of series resistance and circuit potential. We now show

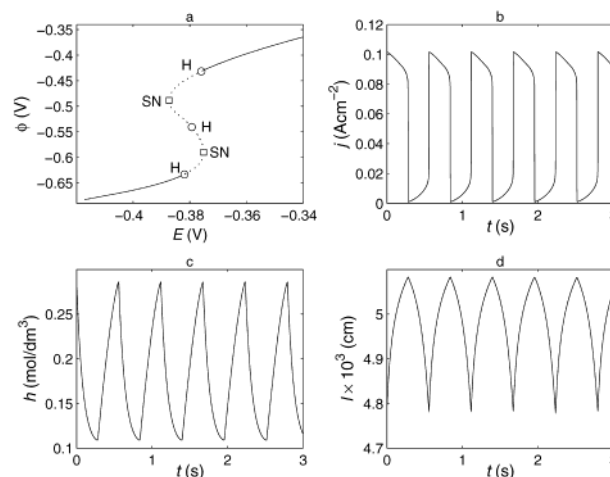


Figure 9. Simulated dynamics in the active–passive oscillatory region at $R_0 = 2.5 \Omega \text{ cm}^2$. (a) Bifurcation diagram showing the position of the steady states and the bifurcation points. Solid line: stable steady state. Dotted line: unstable steady-state. Circle: Hopf bifurcation. Square: saddle-node bifurcation. (b–d) Time series data at $E = -0.38 \text{ V}$: (b) current density; (c) hydrogen ion; (d) salt layer thickness.

representative time series and bifurcation diagrams in each of these qualitatively different dynamical regions.

With very small resistance, oscillations are not observed, as was seen in Figure 8a; a minimal resistance is required for oscillatory behavior. The need for a minimal resistance is a characteristic of negative differential resistance (NDR) electrochemical oscillators.^{21,49} In this type of oscillator, there is a negative slope of the polarization curve in the $R \rightarrow 0$ limit. With some resistance and in the presence of additional (usually slow negative feedback provided by some slow mass-transfer process or a slow chemical reaction) processes, oscillations can occur. With small resistance (Figure 8a) we see two negative slopes on the polarization curve: one on the mass-transfer region due to changes in salt layer film porosity and one due to passivation. Therefore, there is a possibility of oscillations in both regions with appropriate external resistors.

Active–Passive Oscillatory Region. Active–passive oscillations on the forward polarization scan are observed with series resistances in the range $2 \Omega \text{ cm}^2 < R_0 < 3.5 \Omega \text{ cm}^2$. A numerical one-parameter bifurcation diagram is shown in Figure 9a at $R_0 = 2.5 \Omega \text{ cm}^2$. (The corresponding polarization scan is presented in Figure 8b.) The system has a stable steady state below $E = -0.3819 \text{ V}$; at this potential the steady state loses its stability through a supercritical Hopf bifurcation. Two additional saddle-node and Hopf bifurcations occur. [The middle branch is a saddle; that is, it has one positive real eigenvalue everywhere. The other three can remain real and negative or can change during subsequent bifurcations. Under the conditions of Figure 9a, two of the negative eigenvalues become complex and the real part then changes sign in a Hopf bifurcation. The Hopf bifurcation on the middle branch was observed in the four-variable model and not in the simplified model with fixed salt layer thickness, $l = \text{constant}$.] For $E \geq -0.376 \text{ V}$ the Hopf bifurcation on the passive branch gives a stable steady state.

A representative oscillatory waveform is shown in Figure 9b–d at $E = -0.38 \text{ V}$. Current oscillations (Figure 9b) are relaxational and undergo slow and fast variations with time. The current density varies between about 0 A cm^{-2} (passive state) and about 0.1 A cm^{-2} (active state). Note that the maximum of the current is larger than that for the limiting current of the mass-transfer region. This is an important characteristic of active–passive oscillations of iron dissolution.

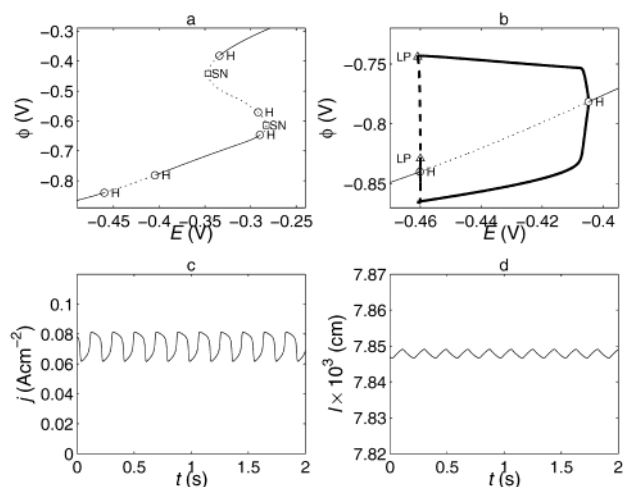


Figure 10. Simulated dynamics in the mass-transfer-limited oscillatory region at $R_0 = 4 \Omega \text{ cm}^2$. (a) Bifurcation diagram showing the positions of the steady states and the bifurcation points. (b) Bifurcation diagram showing periodic and steady-state attractors. Solid line: stable steady state. Dotted line: unstable steady state. Thick solid line: maxima and minima of the stable limit cycle. Thick dashed line: maxima and minima of the unstable limit cycle. Circle: Hopf bifurcation. Square: saddle-node bifurcation. Triangle: limit point of periodic orbits. (c–d) Time series data at $E = -0.43 \text{ V}$: (c) current density; (d) salt layer thickness.

Right after activation, the salt-film layer is thin (see Figure 9d); thus, the current can be higher than the mass-transfer-limited value with a thick (steady) salt film. However, after the activation, the current slowly decreases to the mass-transfer-limited region as the salt-film thickness increases. The hydrogen ions transfer most of the current, causing a decrease of concentration on the electrode surface (Figure 9c). An increase in pH shifts the Flade potential, and the electrode passivates. The oscillation waveform and the characteristics of the oscillations follow the original Franck–FitzHugh ideas;³¹ similar oscillation waveforms and bifurcation diagrams were obtained by Koper and Sluyters with a modified Frank–FitzHugh model incorporating ohmic drop and a simplified salt layer formation model.³⁹

Oscillations in the Mass-Transfer-Limited Region. At $R_0 = 4 \Omega \text{ cm}^2$ there are two main changes in dynamics compared to that obtained with lower resistance ($R_0 = 2.5 \Omega \text{ cm}^2$). There is a new oscillatory region on the mass-transfer-limited region (Figure 8c), and there are no active–passive oscillations. The bifurcation diagram is shown in Figure 10a. A new oscillatory region is observed at lower potentials bracketed by supercritical Hopf bifurcations at $E = -0.4601 \text{ V}$ and $E = -0.4048 \text{ V}$. A detailed figure of the steady-state and periodic solutions in this region is presented in Figure 10b. The low potential drop (high current) steady-state loses its stability through a Hopf bifurcation at $E = -0.4601 \text{ V}$, and a stable small amplitude periodic solution arises above it. There are two limit points (saddle-node bifurcations) of periodic orbits in a very narrow region of circuit potential; above this region a stable periodic solution is obtained. Time series of current density and salt layer thickness at $E = -0.43 \text{ V}$ are shown in Figure 10c and d, respectively. The amplitude of oscillations is smaller and the frequency is larger than those of the relaxation region. The oscillations cease through a supercritical Hopf bifurcation at $E = -0.4048 \text{ V}$. At larger potentials ($E > -0.4 \text{ V}$) the bifurcation diagram (Figure 10a) is similar to that shown for the relaxation oscillatory region in Figure 9a. Note, however, that the Hopf bifurcation of the low potential (active state, E_{Hopf}

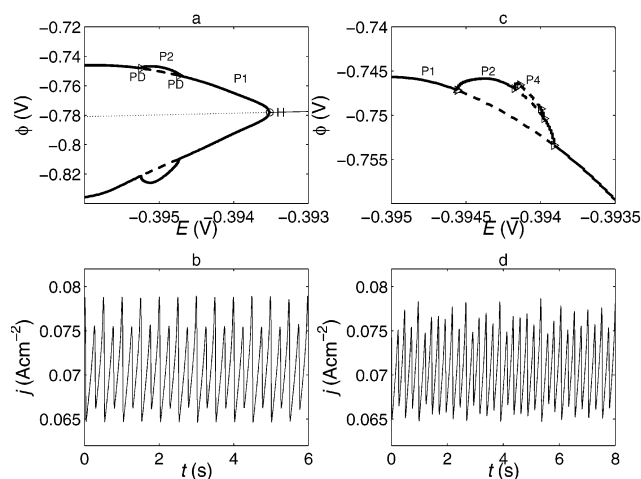


Figure 11. Simulations. Period doubling route to chaos in the mass-transfer-limited oscillatory region. (a) Bifurcation diagram at $R_0 = 4.117 \Omega \text{ cm}^2$. (b) Period-2 current oscillations at $R_0 = 4.117 \Omega \text{ cm}^2$ and $E = -0.395 \text{ V}$. (c) Bifurcation diagram at $R_0 = 4.125 \Omega \text{ cm}^2$. (d) Chaotic current oscillations at $R_0 = 4.125 \Omega \text{ cm}^2$ and $E = -0.3941 \text{ V}$. Notation is as in Figure 10. Right triangle: period-doubling bifurcation. P_n denotes a period- n solution, where $n = 1, 2$, or 4.

$= -0.2898 \text{ V}$) state occurs at a larger potential than that for the Hopf bifurcation of high potential (passive state, $E_{\text{Hopf}} = -0.3340 \text{ V}$); therefore, during a polarization scan the passive state is already stable before the Hopf bifurcation at -0.2898 V is reached. Thus, during the forward scan the system simply passivates at the Hopf bifurcation. We note that traditionally the system is expected to passivate at the first SN bifurcation that occurs at $E = E_{\text{Flade}} + jR$.⁵⁰ However, due to the complex dynamics of iron dissolution, the passivation occurs at a lower potential. This early passivation was observed in all simulations with larger resistors ($R_0 \geq 3.5 \Omega \text{ cm}^2$) as well as in the experiments.

In the mass-transfer oscillatory region at $R_0 = 4 \Omega \text{ cm}^2$ the oscillations are periodic. Just above $R_0 = 4 \Omega \text{ cm}^2$, more complex behavior occurs close to the Hopf bifurcation at the larger potential. The development of chaotic behavior is shown in Figure 11. At $R_0 = 4.117 \Omega \text{ cm}^2$ the period-1 oscillations lose their stability in a narrow region of circuit potential through period-doubling bifurcations, and period-2 oscillations are observed (Figure 11a and b). At $R_0 = 4.125 \Omega \text{ cm}^2$ a period-doubling cascade to chaotic behavior is obtained (Figure 11c and d); the amplitudes of the chaotic oscillations are similar to those of the periodic oscillations seen at lower resistance. The experimental time series in the mass-transfer region are typically chaotic; the model does show chaotic oscillations in a relatively narrow region of applied potential.

Bursting Oscillations. The dynamics above $R_0 = 4.125 \Omega \text{ cm}^2$ become very complex. Figure 12a is a bifurcation diagram of the mass-transfer-limited region at $R_0 = 5 \Omega \text{ cm}^2$. The periodic oscillations lose their stability through a period-doubling bifurcation. Over most of the region (dashed line of Figure 12a) the time series of current densities (Figure 12c) and the salt-film layer (Figure 12d) exhibit complicated waveforms. The current oscillations consist of a series of high frequency, very small amplitude oscillations and one slower, large amplitude cycle; the amplitude of the single, slower spike is similar to those seen in the mass-transfer oscillations in Figure 10c. The alternate occurrence of such oscillations was also seen in the experiments (Figure 5c). The salt layer thickness gradually increases during the small amplitude oscillatory region and suddenly drops during the large amplitude oscillations. These

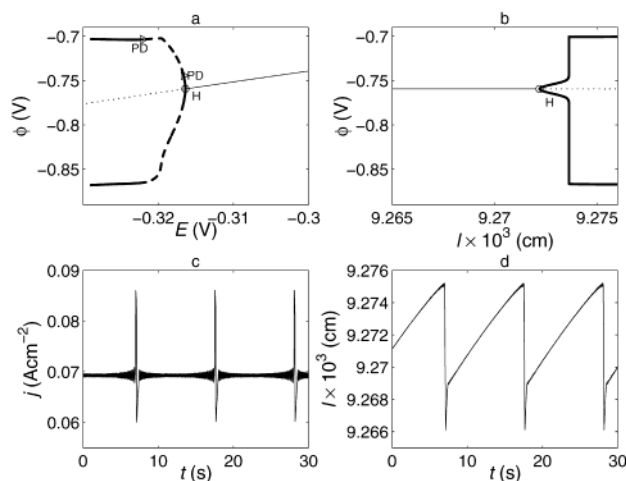


Figure 12. Simulations. Bursting dynamics in the mass-transfer oscillatory region at $R_0 = 5 \Omega \text{ cm}^2$. (a) Bifurcation diagram with E as the parameter. (b) Bifurcation diagram obtained at $E = -0.3167 \text{ V}$ with l as the bifurcation parameter. The notation is the same as that in Figure 10. (c and d) Time series data at $E = -0.3167 \text{ V}$. (c) Current density. (d) Salt layer thickness.

variations are characteristic of bursting dynamics in which oscillations of widely different time scales are observed.

Bursting oscillators are often studied by taking the slow variable as a fixed parameter; there are often bifurcations leading to abrupt changes as the slow variable is changed. Figure 12b shows the bifurcation diagram of the system at $E = -0.3167 \text{ V}$ (corresponding to the time series of Figure 12c and d) as a function of the slow variable, the salt layer thickness; the salt layer thickness is held constant, and the three-variable system (eqs 7a–c) is solved. There is a Hopf bifurcation at $l = 9.2722 \times 10^{-3} \text{ cm}$ and an abrupt change of the amplitude at $l = 9.2736 \times 10^{-3} \text{ cm}$. Such an abrupt change is called a “canard” bifurcation;⁵² although there is no actual bifurcation, the dynamics changes almost discontinuously. Therefore, the bursting dynamics can be interpreted as an alternation between high and low amplitude oscillatory regions due to small changes in the salt-film thickness.

Another type of bursting oscillation is observed with even larger resistance, $5 \Omega \text{ cm}^2 \leq R_0 \leq 6.5 \Omega \text{ cm}^2$. The bifurcation diagram at $R_0 = 6 \Omega \text{ cm}^2$ is shown in Figure 13a. The same local bifurcations of the steady state as seen in Figure 10a (at $R_0 = 4 \Omega \text{ cm}^2$) are observed; however, their relative positions have changed. The bifurcation structure is shifted to larger potentials compared, for example, to those of Figure 10a; however, due to the large IR drop in the mass-transfer region, the lower branch (high current) is shifted more than the upper branch. Thus, the mass-transfer oscillatory region is moved closer to the active–passive region. Time series of current density and salt layer thickness are shown at $E = -0.32 \text{ V}$ in Figure 13c and d. In the current there is an alternation of a series of small amplitude, fast oscillations and one large amplitude oscillation during which the electrode passivates. The salt layer film builds up until passivation, at which point it decreases. Figure 13b shows the maxima of oscillations at $E = -0.32 \text{ V}$ as a function of salt layer thickness. The quantity l is again assumed to be a parameter and the three-variable system solved. Hysteresis with large and small amplitude oscillations is observed. The bursting oscillations of Figure 13c are thus due to the alternation of small amplitude (mass-transfer) and large amplitude (active–passive) oscillations. The bursting is associated with a hysteresis as a function of the salt layer thickness. At larger potentials, such as $E = -0.31 \text{ V}$ (Figure

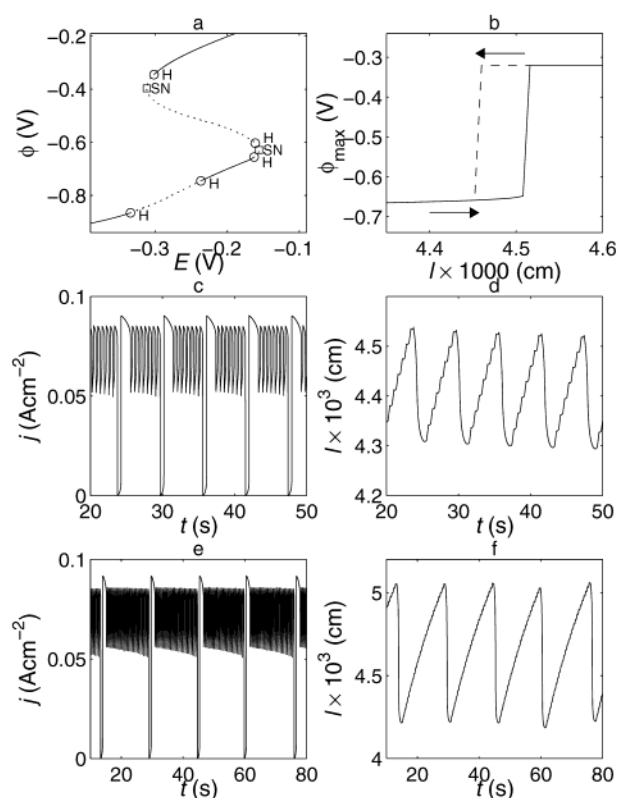


Figure 13. Simulations. Bursting dynamics in the mixed active–passive and mass-transfer oscillatory region at $R_0 = 6 \Omega \text{ cm}^2$. (a) Bifurcation diagram with E as the parameter. Notations are the same as those in Figure 10. (b) The maxima of potential oscillations at fixed salt layer thickness as a function of l . Results are shown for scanning the l up (solid curve) or down (dashed curve). $E = -0.32 \text{ V}$. (c and d) Time series data at $E = -0.32 \text{ V}$: (c) current density; (d) salt layer thickness. (e and f) Time series data at $E = -0.31 \text{ V}$: (e) current density; (f) salt layer thickness.

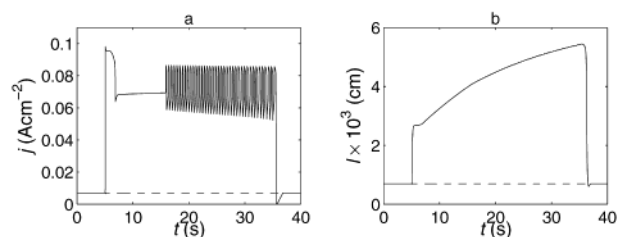


Figure 14. Simulations. The effect of sub- and suprathreshold potential perturbations at $R_0 = 6 \Omega \text{ cm}^2$ and $E = -0.301 \text{ V}$. The steady-state potential $\phi_{ss} = -0.343 \text{ V}$ is perturbed by 5 (solid curve) and 4.9 mV (dashed curve) at $t = 5 \text{ s}$. (a) Current density as a function of time. (b) Salt layer thickness as a function of time.

13e and f), the bursting region is longer. With further increasing the potential, passivation occurs from bursting behavior. These bursting dynamics exhibit similarities to the experimental behavior shown in Figures 2d, 3a and b, and 4b and c.

In the high resistance region (e.g., $R_0 = 6 \Omega \text{ cm}^2$) very long transients are observed. After a change in potential, it takes a long time for the system to reach a stationary (either steady or oscillatory) state. Excitability with long oscillatory transients (Figure 14) similar to that seen in the experiments (Figure 7) is obtained. At a circuit potential of $E = -0.301 \text{ V}$, the passive steady state is stable. At $t = 5 \text{ s}$ the variable ϕ was perturbed by 4.9 mV. This subthreshold perturbation does not have an important effect on the dynamics (dashed line); the system quickly relaxes back to the steady state. However, a 5 mV perturbation activates the electrode (solid line), after which there

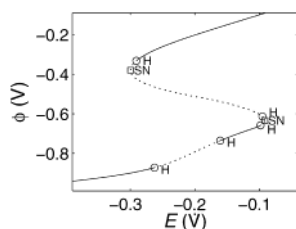


Figure 15. Simulated bifurcation diagram at $R_0 = 7 \, \Omega \, \text{cm}^2$. Notation is the same as that in Figure 10.

is a long transient of about 30 s (involving ca. 40 transient oscillations) before the system relaxes to the steady state. As shown in Figure 14b, during this transient, the salt film builds up and then breaks down.

With very large resistance, no oscillations are observed on the forward scan (See Figure 8f at $R_0 = 7 \, \Omega \, \text{cm}^2$.) The passivation occurs at relatively low potentials close to the top of the polarization curve where the current drops due to salt layer formation and changes in porosity. In the corresponding bifurcation diagram (Figure 15) the region of instabilities on the mass-transfer plateau is shifted into the active–passion region to such an extent that the first Hopf bifurcation on the active branch ($E = -0.2626 \, \text{V}$) is at a higher potential than that for the Hopf bifurcation on the passive branch ($E = -0.2907 \, \text{V}$). Therefore, as soon as the system reaches the Hopf bifurcation on the forward scan, it passivates. The passive state is stable; no stable oscillatory state around the lower branch is observed. Bursting oscillations do not develop because the system does not reactivate following excursions to the passive state.

5. Discussion

In electrochemical systems there are easily controllable parameters, for example, external resistance and circuit potential, that enable the study of dynamics, such as the emergence and disappearance of bursting. The complex dynamics of the electrodisolution of iron were studied with relatively large external resistance. With appropriate external resistance, bursting oscillations were observed. The experimentally observed bursting behavior has some interesting properties. The slow dynamics over which the repetitive spiking is observed is inherently chaotic. Thus, the simple classification based on periodic bursting⁶ may not directly apply. In addition, the length and the occurrence of bursting intervals are irregular, leading to chaotic bursting. The occurrence rate and the length of bursting intervals increase with increase in potential; thus, longer parts of the chaotic oscillation are filled with bursts. At larger bursting intervals the chaotic slow dynamics is suppressed and regular bursting is observed. The bursting dynamics thus can play a kind of regulator of the chaotic inherent dynamics. The regular periodic bursts typically disappear through a period lengthening process similar to a homoclinic bifurcation. (Period lengthening was observed in bursters with time delay.⁵³) The occurrence of periodic bursting depends on system parameters such as resistance, electrolyte concentration, and surface area of the electrode.

The dynamics depends strongly on an external resistance that changes the IR drop in the system. We can expect similar dynamical behavior with change in other parameters that influence the IR drop. Two such parameters would be the mass-transfer coefficient near the electrode surface (varied by an impinging jet velocity or a disk rotation rate) and the working electrode surface area. With an increasing mass-transfer rate,

the IR drop increases due to the increase in current, and thus, bursting dynamics would be expected to occur without external resistance. Similarly, a larger electrode size can increase the IR drop. The occurrence of “noisy”, high frequency oscillations has been pointed out by Russel and Newman.²³ They observed that these oscillations occur more frequently with larger electrodes at larger rotation rates. A subsequent detailed study of mass-transfer oscillations revealed that the complexity of oscillations increases with surface area and complex (high dimensional chaotic) oscillations occur at high rotation rates.⁵⁴ We note that in these experiments the coupling in the system is also changed with increased electrode size; thus, it is possible that both synchronization and local dynamics are affected by a change in electrode size.

It is well-known that the activation and passivation potentials of iron in sulfuric acid solution differ because of the combined effect of the IR drop in the solution and the increased pH of the electrode surface on the active branch of the polarization curve.^{46,50} However, the passivation with a large IR drop can occur at more cathodic potentials because of a loss of stability of the active branch. Passivation then occurs from a state of oscillatory bursting or, at extreme resistance values, from steady-state behavior close to a potential where instabilities on the mass-transfer plateau arise. Therefore, even to interpret a simple but practically important quantity such as the passivation potential, a detailed knowledge of the dynamics is required.

The model developed here describes the essential dynamical features of a well-studied electrochemical reaction system: iron electrodisolution in sulfuric acid solution. It exhibits slow active–passive oscillatory behavior, fast mass-transfer plateau periodic and chaotic oscillations, as well as two types of bursting. The model interprets the effect of resistance on the dynamics of metal dissolution processes. An important feature is the incorporation of a slow variable, the thickness of a salt film. Although the variations of the salt film are slow and small, this variation has a substantial effect on the overall dynamics of the system; variations past bifurcation points of the subsystem (constant salt film) can produce abrupt changes in the overall dynamics. Such effects most likely can be seen in other metal dissolution systems. Burstinglike behavior with long transients has been indeed observed during copper dissolution in acidic chloride media where a copper(I) chloride film forms.⁵⁵

Bursting oscillations in the iron dissolution system have many features that have been observed in neuronal pacemakers; therefore, the electrochemical system can serve as a model system. Neurons typically coupled together to form a population. Coupling in electrochemical systems can also be controlled both on a single surface⁴⁹ or on an array of electrodes.^{56,57} The interaction is through the potential drop in the electrolyte or on a resistance in the external circuitry. This model system provides an experimentally feasible way to explore some synchronization properties of bursting oscillators that are more difficult to study directly in the biological systems.

Acknowledgment. This work was supported in part by the National Science Foundation (CTS-0000483) and the Office of Naval Research (N00014-01-1-0603).

Note Added after ASAP Posting. This article was posted ASAP on 6/17/2003. A change has been made to eq 6. The correct version was posted on 6/19/2003.

References and Notes

- (1) Rinzel, J. A Formal Classification of Bursting Mechanisms in Excitable Systems. In *Mathematical Topics in Population Biology, Morphogenesis and Neurosciences*; Springer: Berlin, 1987; p 267.

- (2) Plant, R. E. *J. Math. Biol.* **1981**, *11*, 15.
- (3) Chay, T. R.; Keizer, J. *Biophys. J.* **1983**, *42*, 181.
- (4) Pernarowski, M.; Miura, R. M.; Kevorkian, J. *SIAM J. Appl. Math.* **1992**, *52*, 1627.
- (5) Del Negro, C. A.; Hsiao, C. F.; Chandler, S. H.; Garfinkel, A. *Biophys. J.* **1998**, *75*, 174.
- (6) Izhikevich, E. M. *Int. J. Bifurcation Chaos* **2000**, *10*, 1171.
- (7) Meucci, R.; Di Garbo, A.; Allaria, E.; Arecchi, F. T. *Phys. Rev. Lett.* **2002**, *88*, 144101.
- (8) Graziani, K. R.; Hudson, J. L.; Schmitz, R. A. *Chem. Eng. J.* **1976**, *12*, 9.
- (9) Dolnik, M.; Epstein, I. R. *J. Chem. Phys.* **1993**, *98*, 1149.
- (10) West, D. H.; Smits, G.; Kotanchev, M.; Mercure, P. K. Chaotic Bursting in an Externally Excited Industrial Reactor. AIChE Annual Meeting, Indianapolis, IN, 2002.
- (11) Fetner, N.; Hudson, J. L. *J. Phys. Chem.* **1990**, *94*, 6506.
- (12) van Venrooij, T. G. J.; Koper, M. T. M. *Electrochim. Acta* **1995**, *40*, 1689.
- (13) Sazou, D.; Diamantopoulou, A.; Pagitsas, M. *J. Electroanal. Chem.* **2000**, *489*, 1.
- (14) Sazou, D.; Diamantopoulou, A.; Pagitsas, M. *Electrochim. Acta* **2000**, *45*, 2573.
- (15) Sazou, D.; Georgolios, C. *Electrochim. Acta* **1996**, *41*, 147.
- (16) Sazou, D.; Pagitsas, M.; Georgolios, C. *Electrochim. Acta* **1993**, *38*, 2321.
- (17) Sazou, D.; Pagitsas, M.; Georgolios, C. *Electrochim. Acta* **1992**, *37*, 2067.
- (18) Pagitsas, M.; Sazou, D. *J. Electroanal. Chem.* **1999**, *471*, 132.
- (19) Georgolios, C.; Sazou, D. *J. Solid State Electrochem.* **1998**, *2*, 340.
- (20) D'Alba, F.; Lucarini, C. *Bioelectrochem. Bioenerg.* **1995**, *38*, 185.
- (21) Koper, M. T. M. *Adv. Chem. Phys.* **1996**, *92*, 161.
- (22) Hudson, J. L.; Tsotsis, T. T. *Chem. Eng. Sci.* **1994**, *49*, 1493.
- (23) Russell, P.; Newman, J. J. *Electrochem. Soc.* **1986**, *133*, 2093.
- (24) Diem, C. B.; Hudson, J. L. *AIChE J.* **1987**, *33*, 218.
- (25) Geraldo, A. B.; Barcia, O. E.; Mattos, O. R.; Huet, F.; Tribollet, B. *Electrochim. Acta* **1998**, *44*, 455.
- (26) Sazou, D.; Diamantopoulou, A.; Pagitsas, M. *Russ. J. Electrochem.* **2000**, *36*, 1072.
- (27) Kleinke, M. U. *J. Phys. Chem.* **1995**, *99*, 9.
- (28) Ferreira, J. R. R. M.; Barcia, O. E.; Mattos, O. R.; Tribollet, B. *Electrochim. Acta* **1994**, *39*, 933.
- (29) Bartlett, J. H. *Trans. Electrochem. Soc.* **1945**, *87*, 521.
- (30) Franck, U. F. Z. *Electrochem.* **1958**, *62*, 649.
- (31) Franck, U. F.; FitzHugh, R. Z. *Electrochem.* **1961**, *65*, 156.
- (32) Podesta, J. J.; Piatti, R. C.; Arvia, A. J. *J. Electrochem. Soc.* **1979**, *126*, 1363.
- (33) Nakabayashi, S.; Zama, K.; Uosaki, K. *J. Electrochem. Soc.* **1996**, *143*, 2258.
- (34) Degn, H. *Trans. Faraday Soc.* **1967**, 1348.
- (35) Orazem, M. E.; Miller, M. G. J. *Electrochem. Soc.* **1987**, 134.
- (36) Rush, B.; Newman, J. J. *Electrochem. Soc.* **1995**, *142*, 3770.
- (37) Hua, D.; Luo, J. *Chem. Phys. Lett.* **1999**, *299*, 345.
- (38) Russell, P.; Newman, J. J. *Electrochem. Soc.* **1987**, *134*, 1051.
- (39) Koper, M. T. M.; Sluyters, J. H. J. *Electroanal. Chem.* **1993**, *347*, 31.
- (40) Murphy, S. V.; Hibbert, D. B. *Phys. Chem. Chem. Phys.* **1999**, *1*, 5163.
- (41) Talbot, J. B.; Oriani, R. A.; DiCarlo, M. J. *J. Electrochem. Soc.* **1985**, *132*, 1545.
- (42) Pagitsas, M.; Sazou, D. *Electrochim. Acta* **1991**, *36*, 1301.
- (43) Wang, Y.; Hudson, J. L.; Jaeger, N. I. *J. Electrochem. Soc.* **1990**, *137*, 485.
- (44) Birzu, A.; Green, B. J.; Otterstedt, R. D.; Jaeger, N. I.; Hudson, J. L. *Phys. Chem. Chem. Phys.* **2000**, *2*, 2715.
- (45) Beck, T. J. *Electrochem. Soc.* **1982**, *129*, 2412.
- (46) Russell, P. P.; Newman, J. J. *Electrochem. Soc.* **1983**, *130*, 547.
- (47) Epelboin, I.; Gabrielli, C.; Keddam, M.; Lestrade, J.-C.; Takenouti, H. *J. Electrochem. Soc.* **1972**, *119*, 1632.
- (48) Koper, M. T. M. *Electrochim. Acta* **1992**, *37*, 1771.
- (49) Krischer, K. Nonlinear Dynamics in Electrochemical Systems. In *Advances in Electrochemical Science and Engineering*; Alkire, R. C., Ed.; Wiley-VCH Verlag: 2002; Vol. 8; p 89.
- (50) Franck, U. F. Z. *Naturforsch.* **1949**, *4a*, 378.
- (51) Gear, C. W. *Numerical Initial Value Problems in Ordinary Differential Equations*; Prentice Hall: Englewood Cliffs, NJ, 1971.
- (52) Eckhaus, W. *Lect. Notes Math.* **1983**, *985*, 449.
- (53) Destexhe, A.; Gaspard, P. *Phys. Lett. A* **1993**, *173*, 386.
- (54) Wang, Y.; Hudson, J. L. *AIChE J.* **1991**, *37*, 1833.
- (55) Bassett, M. R.; Hudson, J. L. *J. Electrochem. Soc.* **1990**, *137*, 922.
- (56) Kiss, I. Z.; Zhai, Y. M.; Hudson, J. L. *Science* **2002**, *296*, 1676.
- (57) Kiss, I. Z.; Wang, W.; Hudson, J. L. *J. Phys. Chem. B* **1999**, *103*, 11433.